

# **Simulating the Measurement of the Electron Beam Emittance at AWAKE**

Patrick Chin

March 24, 2017

Supervised by Prof. M. Wing  
& Dr. S. Jolly

## Abstract

In preparation for runs at AWAKE in CERN, simulations of the beam and measurement of beam parameters with a spectrometer were carried out. This was done in order to investigate how the spectrometer behaves under changes to experimental parameters. The energy spreads of the beam were tested and a percentage energy spread of 4 % was found to be the cutoff point at which measurements become reliable. Emittance values were tested and emittances above  $10^{-5}$  mrad were found to be inaccurate. Background photon values up to  $10^4$  times the expected background were simulated, showing accurate measurements up to a factor of  $\sim 4 \times 10^2$ , above which the measured emittance deviated significantly from the true value.

# Contents

<b>1</b>	<b>Introduction</b>	<b>1</b>
<b>2</b>	<b>Plasma Wakefield Acceleration</b>	<b>1</b>
2.1	Self-modulation instability . . . . .	1
2.2	Uniform-density plasma cell . . . . .	2
2.3	Injection of the witness beam . . . . .	2
<b>3</b>	<b>AWAKE</b>	<b>2</b>
<b>4</b>	<b>Spectrometer</b>	<b>3</b>
<b>5</b>	<b>Theory</b>	<b>3</b>
5.1	Single Particle Dynamics . . . . .	3
5.2	Emittance . . . . .	3
<b>6</b>	<b>The Simulation</b>	<b>4</b>
6.1	The Electron Beam . . . . .	4
6.1.1	BDSIM Calibration . . . . .	4
6.1.2	Deriving the Beam Size Function . . . . .	5
6.2	Backgrounds . . . . .	6
6.2.1	Error Calculations . . . . .	7
6.3	Calculating the Emittance . . . . .	7
<b>7</b>	<b>Results</b>	<b>7</b>
7.1	Binning errors . . . . .	7
7.2	Energy Spread . . . . .	8
7.3	Input Emittance . . . . .	10
7.4	Background Photons . . . . .	10
<b>8</b>	<b>Conclusion</b>	<b>10</b>
8.1	Errors . . . . .	10
8.2	Parameters . . . . .	10

# 1 Introduction

Advancements in quantum and particle physics are primarily driven by experimental observations which can verify or refute previous hypotheses, or can provide data from which new hypotheses can be drawn. Particle colliders are a main source of observational data at the quantum scale, and can create millions of collision events every second. Design modifications to these colliders mostly increase the luminosity of the collision in order to increase the collision rate and produce more data. This report however, focuses on a design modification aimed at increasing the energy of the colliding beams.

Proton-proton beam energies at the Large Hadron Collider (LHC) have recently reached energies of 13 TeV [6], whereas lepton-lepton colliders have yet to reach the TeV energy scale. The largest of lepton-lepton, the Large Electron-Proton Collider (LEP), was closed down to make way for the LHC in 2000 after having reached a maximum energy of 209 GeV [3].

One of the drawbacks to circular accelerators, is the loss of a particle's energy due to synchrotron radiation. This is the emittance of radiation from relativistic charged particles that are moving in a uniform magnetic field. The energy loss is inversely proportional to the fourth power of the rest mass of the particle [16], meaning that electrons lose more energy than protons by a factor of about  $10^{13}$  which is. During experiments performed at the LEP the radiated power when running at 100 GeV reached about 18 MW which needs to be resupplied to the beam.

There are currently two RF linear lepton accelerator proposals, the Compact Linear Collider (CLIC) and the International Linear Collider (ILC) which are expected to reach collision energies of up to several TeV and 500 GeV respectively. Both collaborations have recently joined efforts under the Linear Collider Collaboration.

Looking further into the future

continuing to increase the energy of colliding beams allows for an increasing number of interactions to be observed.

# 2 Plasma Wakefield Acceleration

Current radio-frequency (RF) accelerator technology is limited to an electromagnetic gradient of about  $100 \text{ MeV m}^{-1}$  due to material breakdown in the walls of the structure. The ability of plasma to sustain very large electromagnetic fields made it a good candidate for a medium within which charged particles can be accelerated. In 1979, the concept of laser plasma acceleration was shown in simulations to be of practical use in accelerators and pulsers [17]. More recently, proof-of-concept experiments implementing laser plasma acceleration have been shown to accelerate electrons to the GeV scale in a cm-scale plasma cell [12, 10], showing results that are consistent with simulations.

## 2.1 Self-modulation instability

The first challenge in the development of this accelerator was getting the length of the proton driver bunch small enough so that resonance occurs with the electrons in the plasma. Typical proton bunches, i.e. those produced by the CERN Super Proton Synchrotron (SPS), have lengths of  $\sim 10 \text{ cm}$  which cannot directly create strong plasma waves at the required wavelength in the mm scale as the Fourier component of the proton beam at the plasma frequency is negligible. Simulations [9] on the compression of these bunches show that reducing the longitudinal phase volume blows up the transverse phase volume. An alternative method would be to split up the proton bunch into a number of micro-bunches to be simultaneously decelerated.

An instability between the beam and the plasma arises from the mutual amplification of the rippling of the beam radius and the plasma wave. This instability tends to destroy the plasma wave as the amplification focuses and defocuses selected slices of the beam. This problem was solved by seeding the self-modulated instability (SMI) with a short electron bunch [11], a laser pulse [15] or a sharp cut in the bunch profile [9]. This will promote a single mode and suppress other modes, including the strongest competing modes, the hosing modes [18] and produce well-separated micro-bunches.

## 2.2 Uniform-density plasma cell

The plasma wavelength is  $\lambda_{pe} \approx 1.26$  mm meaning that the 10 cm proton bunch will have to be split into  $\sim 100$  micro-bunches in order to be able to drive the wake. Each micro-bunch contributes to the wake-field, and only if the plasma density is uniform will the contribution of each bunch be coherent. Incoherence will cause the electron bunches to arrive at the wrong phase in the plasma oscillation. An increase in the plasma density will shorten the plasma wavelength causing the electron bunch to crest plasma wave it was riding and fall into the defocusing phase of the plasma wave as shown in Fig 1(a). A decrease in the plasma density will increase the plasma wavelength causing the plasma wave to fall further behind the electron bunch meaning the electron bunch to fall into the trough of the plasma wave resulting in a deceleration of the electron beam 1(c). The electron beam must be in the region of length  $\lambda_{pe}/4$  between the defocusing and decelerating phases of the plasma wave.

This requirement of the plasma limits the plasma selection to being uniform rubidium vapor, ionised by a co-propagating laser pulse [13, 14]. Rubidium was chosen due to it's low ionization potential and heavy atomic mass. A heavy element is required to minimize the movement of the plasma's nuclei which causes adverse effects on the plasma's behaviour [20, 19]. The Rubidium vapor is kept in thermodynamic equilibrium at a constant temperature and volume.

## 2.3 Injection of the witness beam

Due to SMI, the shape of the drive beam changes in the plasma and for the first four meters, the difference between the phase velocity of the wake-field and the proton beam velocity is quite large and this will effect the electron beam in the same manner as having a non uniform plasma, detailed above. To avoid this problem it was suggested that the electrons could be injected into the plasma after SMI had fully developed. The design of the injection method arrived at passing the electron beam through a narrow vacuum tube separated from the plasma by a thin foil. Then after  $\sim 4$  m the electrons will be directed into the wakefield close behind the proton driving beam.

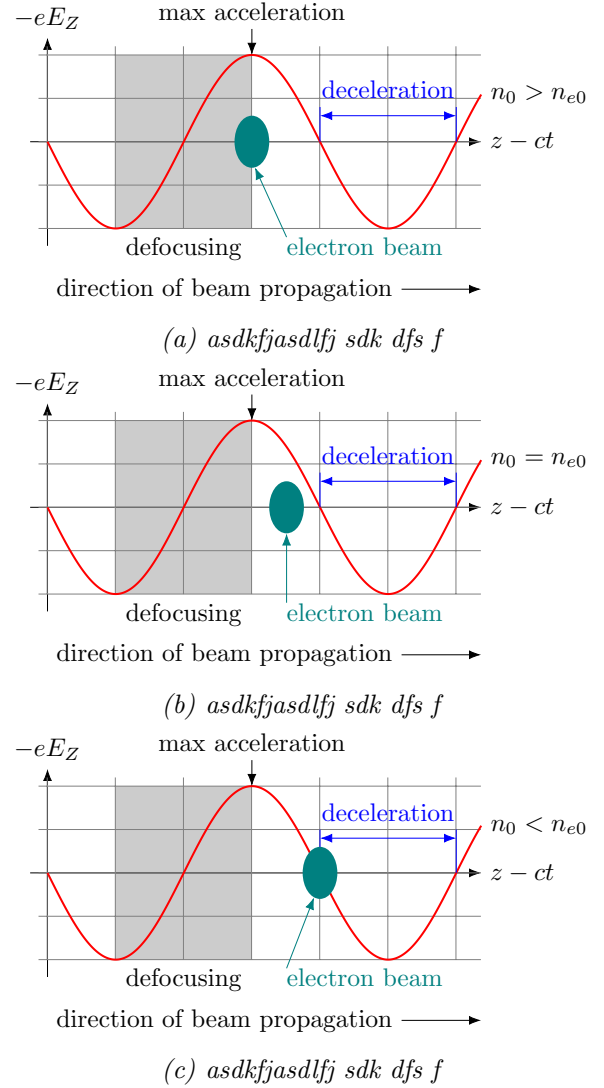


Figure 1: Phasing of the electron bunch for increased density (a) correct density (b) and decreased density (c). [21]

## 3 AWAKE

The aim of this experiment is to provide a proof-of-concept for proton driven plasma wakefield acceleration to be able to accelerate electrons beams to the TeV energy scale. An overview of the experiment as described in the AWAKE design overview: *AWAKE, The Advanced Proton Driven Plasma Wakefield Acceleration Experiment at CERN* [7] is as follows:

The CERN Super Proton Synchrotron (SPS) will provide a 400 GeV proton beam with a bunch length of  $\sigma_z = 12$  cm and an intensity of  $\sim 3 \times 10^{11}$  protons per bunch. This will travel down the 750 m long proton beam line, previously used for the CERN Neutinos to Gran Sasso project (CNGS), and be focused to a horizontal and vertical rms size  $\sigma_{x,y} = 200 \mu\text{m}$  before entering a 10 m long Rubidium vapor plasma

cell with an adjustable density at the  $10^{14}$  to  $10^{15}$  electrons/cm scale.

The proton driver will self modulate at the plasma wavelength  $\lambda_{pe}$  after being seeded by a high powered  $\approx 4.5$  TW laser pulse that is co-axial and co-propagating with the proton driver beam. This laser also serves the purpose of ionising the Rubidium vapor to create the plasma. For these beams to be co-axial for the full length of the plasma cell, they need to be synchronous to within 100 ps and the size of the focal point of the proton beam is required to be  $\leq 100 \mu\text{m}$  and  $\leq 15 \mu\text{rad}$

The electron witness beam will be created via photo-emission by an illuminating cathode electron source and accelerated by a 2.5 cell RF-gun and a meter long booster at 3 GHz.

## 4 Spectrometer

There are two main goals the spectrometer is expected to fulfill. The first is to measure the mean energy and energy spread of the beam as is it this measurement of the mean energy that determines the success of the AWAKE project, whether or not The spectrometer is also

## 5 Theory

### 5.1 Single Particle Dynamics

When working with beams of particles, it is advantageous to work in the coordinate system that follows the ideal path of the beam. If the beam's motion in the  $x$  and  $y$  planes are independent, i.e. we ignore coupling terms, the each particle's motion in each plane can be described by

$$\begin{pmatrix} u(z) \\ u'(z) \end{pmatrix} = \begin{pmatrix} C_u(z) & S_u(z) \\ \sqrt{C'_u(z)} & S'_u(z) \end{pmatrix} \begin{pmatrix} u_0 \\ u'_0 \end{pmatrix} \quad (1)$$

where  $u$  is either  $x$  or  $y$  and  $u'$  is the transverse velocity of the particle in the  $u$  plane. The coordinate  $(u, u')$  lies in what is known as phase space. Using this system of matrices the drift and quadrupole matrices can be derived [21]. The drift matrix is

$$\mathcal{M}_D(l) = \begin{pmatrix} 1 & l \\ 0 & 1 \end{pmatrix} \quad (2)$$

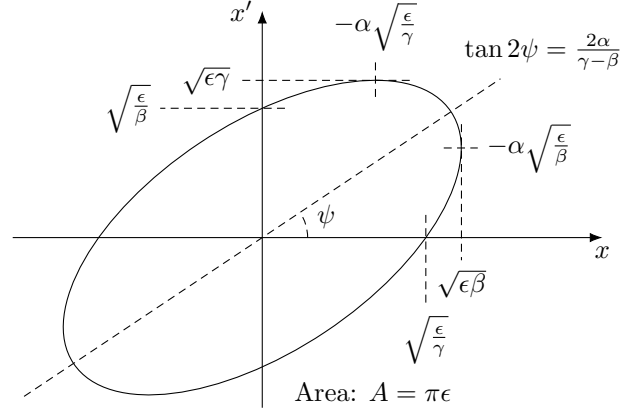


Figure 2: A representation of the relation between the Twiss parameters of a beam's ellipse in phase space [21].

the focusing quadrupole matrix is

$$\mathcal{M}_{QF}(l) = \begin{pmatrix} \cos \psi & \frac{1}{\sqrt{k}} \sin \psi \\ -\sqrt{k} \sin \psi & \cos \psi \end{pmatrix} \quad (3)$$

and the defocusing quadrupole matrix is

$$\mathcal{M}_{QD}(l) = \begin{pmatrix} \cosh \psi & \frac{1}{\sqrt{|k|}} \sinh \psi \\ -\sqrt{|k|} \sinh \psi & \cosh \psi \end{pmatrix} \quad (4)$$

These transport matrices can be multiplied together resulting in the transformation matrix representing a path containing all accelerator components making it simple to follow a particle through a transport line.

### 5.2 Emittance

Grouping the individual particles in a particle beam, they will occupy an area in phase space known as the emittance. Qualitatively the emittance of a beam is a measure of how parallel the particles of the beam are to each other. It is a conserved quantity while the beam is not being acted upon by external forces.

In phase space the beam of particles will usually take up an area resembling that of an ellipse. This is because, after a diverging or converging beam has traveled through an aperture, we expect particles that are further away from the centre of the beam to have a larger transverse momentum. This is unless the beam is being measured at it's waist where it is transitioning between converging and diverging or visa versa. Figure 2 shows the projection of a diverging beam onto a two dimensional phase plane, called the phase ellipse. The line that defines the

ellipse is drawn such that 95 % of all the particles in the beam are contained [5]. The emittance is defined by the area of this ellipse divided by  $\pi$  in units of mrad. Note that in general the transverse momenta, hence the slope of the particles in the beam, are very small so the approximation  $\sin u' \approx u'$  can be used.

The general equation of an ellipse can be used to describe the phase ellipse:

$$\gamma x^2 + 2\alpha x x' + \beta x'^2 = \epsilon \quad (5)$$

where  $\alpha$ ,  $\beta$ ,  $\gamma$  and  $\epsilon$  are ellipse parameters that determine the ellipse's shape and orientation in phase space, where  $\epsilon$ , the area of the ellipse is the emittance<sup>1</sup>. Of the four beam parameters, only three are independent and since  $\epsilon$  is defined as the area, the other three can be found to be correlated from the ellipse's geometric properties by

$$\beta\gamma - \alpha^2 = 1 \quad (6)$$

By expressing this ellipses as a matrix, transformation rules have been derived to transport the beam [21]. The beam matrix can be defined by

$$\sigma = \begin{pmatrix} \sigma_{11} & \sigma_{12} \\ \sigma_{21} & \sigma_{22} \end{pmatrix} = \epsilon \begin{pmatrix} \beta & -\alpha \\ -\alpha & \gamma \end{pmatrix} \quad (7)$$

where each element describes distributions of particles in the beam as follows:

$$\sigma_{11} = \langle x_i^2 \rangle = \epsilon\beta \quad (8)$$

$$\sigma_{22} = \langle x_i'^2 \rangle = \epsilon\gamma \quad (9)$$

$$\sigma_{12} = \langle x_i x_i' \rangle = -\epsilon\alpha \quad (10)$$

The evolution of this matrix along the beam transport line can then be described by

$$\sigma_1 = \mathcal{M} \sigma_0 \mathcal{M}^T \quad (11)$$

## 6 The Simulation

The simulation of this experiment was split into three parts: the simulation of the beam, the simulation of the effects of the background and camera, and the reconstruction of the beam to measure the parameters of the beam.

<sup>1</sup>Often, the units of  $\pi$  are omitted and the emittance is given in units of  $\pi$  mrad.

Parameter	Expected value
Emittance $\epsilon$	$1 \times 10^{-6}$ mrad
Mean energy $\bar{E}$	1.3 GeV
Energy spread $\sigma_E$	0.4 GeV
N. electrons $N_{e-}$	$1 \times 10^9$
Bg. photons	$3.415 \times 10^4$ m <sup>-2</sup>

Table 1: The expected values for many experimental parameters have been calculated. It should be noted that these values are missing error values. It can be assumed that the error on each value can be given by half the least significant digit.

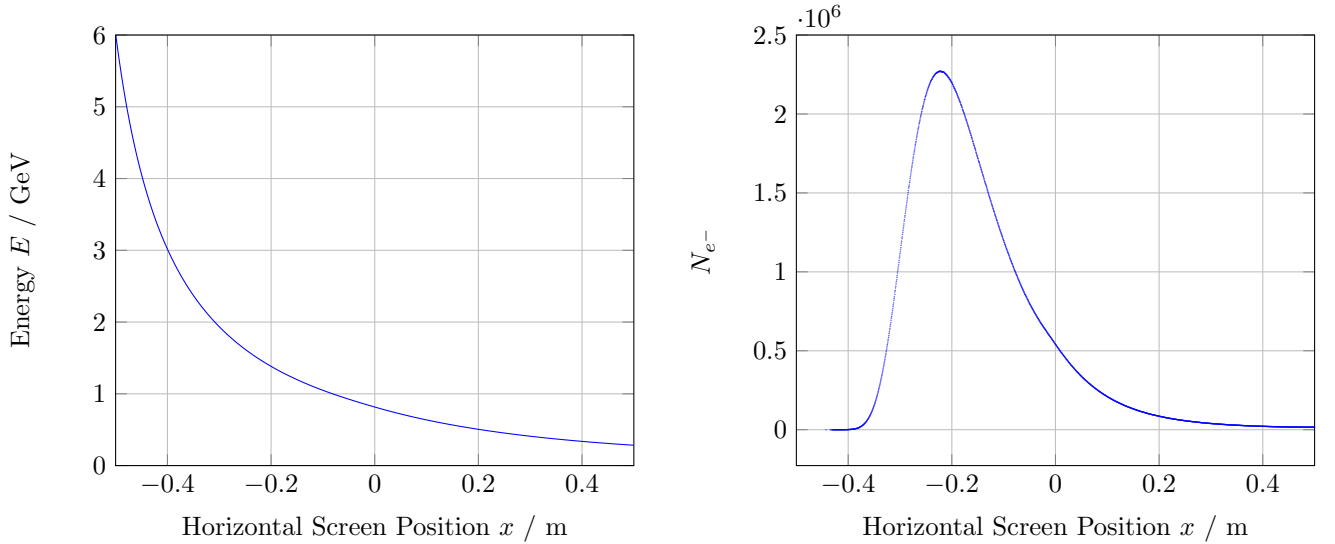
### 6.1 The Electron Beam

Given enough computing power and time, the simulation of the beam from, the end of the plasma cell, passing through two quadrupoles and through a dipole could have been done on BDSIM [1], a Geant4 [2] toolkit for simulating radiation traveling through an accelerator. This software package simulates a each particle individually, updating it's position and velocity at each step through the accelerator by applying the effect of forces from all fields within the accelerator. For beams consisting of  $\sim 10^9$  particles, tracking each particle individually as they travel down the beam line would take enormous amounts of time and available computing power, and as many simulations were required to be performed this would have been impractical for obtaining any reasonable amount of data.

A new program was written, taking advantage of beam matrices to describe the beam as a whole. The goal of the first part of this program is to simulate the intensity of the incident beam at each pixel on the screen.

#### 6.1.1 BDSIM Calibration

The effect of the quadrupole and the dipole are dependant on the energy of the individual electrons in the beam. So to calculate the density of an electrons along with their energies as a function of the horizontal screen position a number of BDSIM simulations were run.  $10^5$  electrons where fired individually down the simulated AWAKE beam line. These electrons had a square energy distribution from 0 TeV to 10 TeV, and had a Gaussian spacial distribution with  $\sigma_x = \sigma_y = 6$  mm, and no transverse momentum hence zero emittance. This large energy range was



(a) Electron energies corresponding to the horizontal screen position due to the effect of the dipole.

(b) The number of electrons expected to hit the screen at each  $x$  position for  $E = 1.3$  GeV and  $\sigma_E = 0.4$  GeV.

Figure 3: The functions  $E(x)$  and  $N_{e-}(x)$  extracted from the BDSIM calibration output data. These functions are used to calculate the horizontal spread of the electrons across the screen.

chosen as to encompass the entire energy range that would hit the screen. The dipole was set to it's highest setting of 650 A to achieve the maximum spread of the beam on the screen.

These BDSIM runs were used to plot the function in Figure 3a which shows the relationship between the electron energy and where is it expected to hit the screen. Figure 3b is an example of the horizontal distribution of a beam of electrons with a Gaussian energy spread onto the screen. This was calculated by applying the inverse of the function  $E(x)$  shown in Figure 3a, to the energy distribution of the beam.

At these experiment settings, the entire of the beam electrons hit the screen allowing for a more accurate measurement of the beam parameters. The effect of the emittance and quadrupoles on the horizontal spread is taken to be negligible in comparison to the effect of the dipole, and so it's effect is taken into account by adding a horizontal smearing to the horizontal position of each electron on the screen. This results in this plot being all that is required to simulate the transverse spread of the beam.

The drift distances from the second quadrupole to the screen were also recorded for each  $x$  position on the screen. This function  $d(x)$  is used in the calculation of the vertical beam size, discussed next.

### 6.1.2 Deriving the Beam Size Function

The dipole spreads the beam horizontally across the screen. The electrons in each vertical strip of pixels are grouped together and their energy approximated to be equal. This is allowed as the energy spread in each strip will always be less than 0.5%. This was calculated from data used to plot Figure 3a, by finding the ratio between the difference in energies between adjacent strips, by the energy value at that strip. This was done for all strips and the maximum value was a 0.5% difference in energy.

Using this assumption, we are able to create one beam and transport matrix for electrons in each vertical stream of pixels. The root mean square of the vertical beam size on the screen can be extracted from the resultant beam matrix  $\sigma_1$ . To arrive at this beam matrix, the transport matrix  $\mathcal{M}$  is applied to the initial beam matrix  $\sigma_0$  in (11). The transport matrix is the product of the transport matrices of each component of the spectrometer:

$$\mathcal{M} = \mathcal{M}_D(d) \cdot \mathcal{M}_{QD}(l_2) \cdot \mathcal{M}_D(g_2) \cdot \mathcal{M}_{QF}(l_1) \cdot \mathcal{M}_D(g_1) \quad (12)$$

where  $\mathcal{M}_D(d)$  is the drift transport matrix which is a function of the travel distance and  $\mathcal{M}_{QD}(l)$  is the transport matrix of the quadrupole.  $g_1$  is the drift distance (the gap) between the end of the plasma cell and the first quadrupole,  $g_2$  is the gap



between the two quadrupoles,  $l_1$  and  $l_2$  are the effective quadrupole lengths of the focusing and defocusing quadrupoles respectively.  $d$  is the drift distance between the second quadrupole and the screen, taking into account the effect of the dipole, hence, is a function of the energy. The shape of this function was calculated in the BSDIM runs.

For simplicity, it is assumed that the quadrupoles strengths  $k_1$  and  $k_2$  are set to values such that each quadrupole focuses at the mean energy of the beam, hence these variables are proportional to the beam's mean energy.

Applying the matrix multiplication results in the vertical beam size as a function of the horizontal screen position:

$$\begin{aligned}\sigma_y^2 = \sigma_{1,11} = & C^2(x)\sigma_{0,11} \\ & + 2C(x)S(x)\sigma_{0,12} \\ & + S^2(x)\sigma_{0,22}\end{aligned}\quad (13)$$

After generating, a two dimensional histogram representing the number of electrons hitting the screen at each pixel the goal is to simulate the effectiveness of the equipment and translate this number to represent the raw signal that will be read off for each pixel.

## 6.2 Backgrounds

How good the measurement of the emittance is, is most dependant on the magnitude of the multiple sources of backgrounds as well as the reliability of the equipment. The following sources of error were taken into account: the efficiency of the scintillator screen, the acceptance of the camera due to it's distance from the scintillator screen, the background photon density, the emittance of photoelectrons in the camera, the thermal noise in the camera, the amplification by the microchannel plate (MCP) and the readout noise. Each source of noise is added to each pixel independently.

The first two error sources, the scintillator screen and the camera acceptance, both scale the signal. So for each electron that hits the screen, it is expected that an average of 5000 photons are to be emitted. The camera acceptance, is the ratio of photons that the camera registers to the number of photons emitted by the scintillator, with a value of  $1.5 \times 10^{-5}$ . After the addition of these two effects, the camera is

expected to receive 7.5 % of the original electron signal. The expected value for the number of photons incident on the camera due to the beam electrons is a Poisson random number.

It is assumed that there is a uniform distribution of photons incident on the camera. The density of these electrons is expected to be  $3.415 \times 10^4$  photons/m<sup>2</sup> equating to 0.01 background photons per pixel during the  $3 \times 10^{-3}$  s the gate is open. The number of background photons that hits a pixel is a discrete value, and so is also generated by generating a Poisson random number. As discussed later in Section 7 this value is very small in comparison to the signal produced by the beam and will only have an effect if the density of background photons is multiple magnitudes larger than the expected value.

The camera's photomultipliers then convert the photons of light back to an electrical current. This multiplies the incident number of photons by the quantum efficiency of the camera, 0.15. thermal photoelectrons per pixel per second is expected to be 0.016 [8], with the camera running at the expected temperature of  $-30^\circ\text{C}$  with  $16^\circ\text{C}$  cooling water and an ambient room temperature of  $16^\circ\text{C}$ . This value is typically doubles for each  $5^\circ\text{C}$  rise in temperature of the camera [8]. At these running temperatures of the camera, about 9 photoelectrons are expected to be generated during the time the gate is open, which is an insignificant proportion in comparison to the beam signal, creating  $1 \times 10^7$  photoelectrons before MCP amplification.

The microchannel plate amplifies the number of photoelectrons by 1442 amplifying all previously added backgrounds. This was simulated by simply scaling the value of the bin, along with it's error, by this value rather than generating a Poisson random number. The modelling of this process may not be reflect the true nature of this process due to an uncertainty in underlying process, however the overall effect remains accurate. Despite this, the error arising from this process is likely to scale the error as mentioned.

And finally, before the values of the signal is obtained, a readout noise is added. This background is expected to add 7.2 readout electrons per image pixel for the camera operating at 1 MHz.

### 6.2.1 Error Calculations

Poisson statistics were used for the calculation of errors. Once the shape of the incident beam on the screen was calculated the number of electrons incident on each pixel was given an error of the square root of the count. Two methods of error propagation were used depending on the nature of the process involved. The following processes were modeled as additive processes: background photons hitting the screen, the thermal electrons from the currents in the camera and the readout noise, whereas the multiplicative processes are: photon generation at the scintillator screen, photoelectron generation in the camera PMTs and the amplification of the electron signal by the MCP.

Basic error propagation techniques were used here. For the additive processes, where the new value of each bin  $n$  is the sum between the old bin value  $n_0$  and the value given by the process  $n_{\text{proc}}$ :  $n = n_0 + n_{\text{proc}}$  the propagation of error is given by calculating the hypotenuse of the absolute errors:

$$\Delta n = \sqrt{\Delta n_0^2 + \Delta n_{\text{proc}}^2} \quad (14)$$

where the error of a Poisson random number is the square root of the value.

For the multiplicative processes, i.e.  $n = \lambda_{\text{proc}} n_0$  where  $\lambda_{\text{proc}}$  is the scaling factor of the process the propagation of the error is given by calculating the hypotenuse of the percentage errors:

$$\Delta n = n \sqrt{\left(\frac{\Delta n_0}{n_0}\right)^2 + \left(\frac{\Delta \lambda_{\text{proc}}}{\lambda_{\text{proc}}}\right)^2} \quad (15)$$

Many of the errors  $\Delta n_{\text{proc}}$  and  $\Delta \lambda_{\text{proc}}$  were unavailable at the time of simulation. All background noises are modeled as uniformly distributed Poisson random numbers so under these assumptions the associated error on each value can correctly be taken to be the square root of the value. For multiplicative processes the resultant values were also Poisson random numbers meaning (15) can be rewritten as

$$\Delta n = n \sqrt{\left(\frac{\Delta n_0}{n_0}\right)^2 + \left(\frac{\sqrt{n}}{n}\right)^2} \quad (16)$$

### 6.3 Calculating the Emittance

The signal received from the camera is required to be scaled back, and background noises removed. This is

done by tracing the beam backwards and subtracting or dividing

The vertical beam size function used to simulate the shape of the incident electron beam is then fit to the measured beam sizes. The fitting is done wholly by CERN ROOT's  $\chi^2$  minimising fitting algorithm [4], using the three beam parameters  $\epsilon$ ,  $\beta$  and  $\gamma$  as parameters to be minimised.

## 7 Results

Along with the  $\chi^2$  minimised parameter values of the fit, each simulation generated a plot, showing the simulated, measured and fitted vertical beam size functions as a function of horizontal position  $x$  on the screen. Figure 4 is the output of a run with all parameters set to their expected values. Figure 5 is an output plot for a run with a small (1 %) energy spread so the spread of the beam is very narrow across the screen, so this plot is essentially zoomed in at a small section of the screen. The solid black line is the shape of the simulated electron beam that hits the screen, the black points show the simulated measurements of the RMS width of the fitted Gaussian for each vertical strip of pixels. The blue dashed line is the beam size function fitted to the points.

### 7.1 Binning errors

After the investigation of multiple experimental parameters, the emittance measurement consistently converged to a value  $1 \times 10^{-8}$  larger than the input emittance. The reason for this systematic error was found to be due to the discretization of the beam hitting the screen meaning that the measurement of the vertical beam size was consistently overestimated. Since the electrons in each pixel are not uniformly distributed but rather more densely distributed closer towards the mean value, giving rise to a systematic overestimation of the vertical beam size of up to two times the vertical size of the pixel. This effect can be seen most clearly when a very small energy spread was used as can be seen in Figure 5, where the measured beam heights are consistently larger than the actual beam height.

This systematic error is displayed in subsequent plots as a blue line, where the red line shows the true beam emittance and the blue line represents

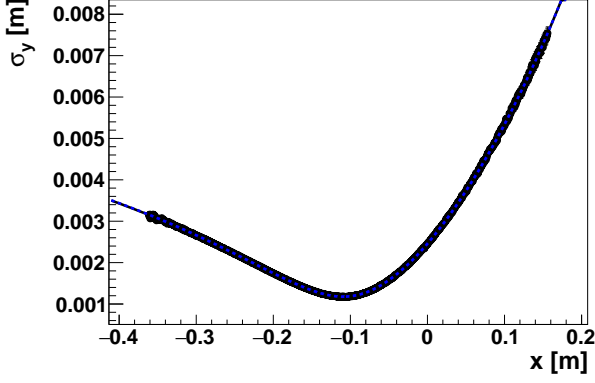


Figure 4: The beam reconstruction (blue line) of a simulation run with all the expected parameter values.  $E = 1.3 \text{ GeV}$ ,  $\sigma_E = 0.4 \text{ GeV}$ ,  $\epsilon = 1 \text{ mm mrad}$

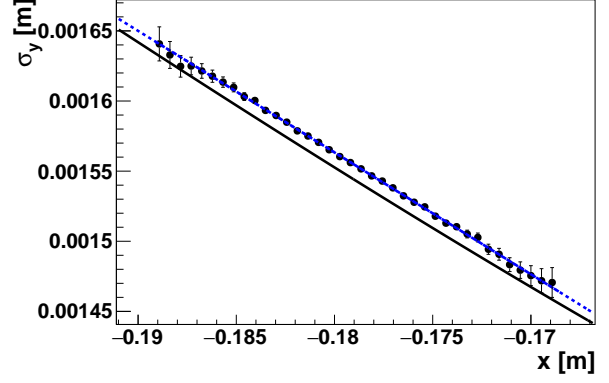


Figure 5: The beam reconstruction, consistently overestimates the vertical beam size. This run used a small percentage energy spread of 1%. With all other parameters set to their expected value.

where the emittance measurement should be taking into account this error.

## 7.2 Energy Spread

Initially, the mean energy of the beam and energy spread of the beam were tested independently. Simulations for all combinations of the following energies  $E \in \{0.5, 1, 1.3, 2.0, 3.05, 6\}$  and the following energy spreads  $\sigma_E \in \{0.01, 0.1, 0.3, 0.4\}$  were run. These energies and energy spreads were chosen such that at least one full standard deviation of the beam hit the screen. As Figure 3a shows, the range of energies that hit the screen for this setting of the dipole and quadrupole, is from  $\sim 0.28 \text{ GeV}$  to  $6 \text{ GeV}$ .

The smaller the energy spread of the beam the smaller the spread of the beam across the screen. Figure 5 is a plot showing the full spread of the beam across the screen for a beam energy spread of 1%. The fewer vertical beam measurements that the function is able to fit to, the larger the errors of fitting will be, so the relationship between the errors of the measured emittance and the energy spread in Figure 6 is the expected result. The expected energy spread,  $0.4 \text{ GeV}$ , translates to a percentage energy spread of 30% at the expected beam energy of  $1.3 \text{ GeV}$ . By this point, the error on the measurement of the emittance has converged to less than a 1%.

Plotting the absolute simulated measurement error against the percentage energy spread in Figure 6 it is clearer the manner in which the errors blow up

for lower energy spreads. For lower energy spreads, all measurement errors were expected to increase exponentially. However this is not the case, but rather, the *spread* of measurement errors increased exponentially, meaning that many measurement errors are still only a few percent of the measurement. This behaviour reflects how the errors for the background noise were calculated; the error associated with the background photons for each pixel is set to the square root of the number of background photons. This means the fewer the number of incident background photons the screen, the smaller the error. However, the error in the uncertainty of the measurement of the background was not taken into account then scaling the raw signal back into the real shape. This extra error arises from the uncertainty in the measurement of the background photon density when there is no accelerated electron beam. To take this into account, this error must be added in quadrature to each pixel.

The upper ranges of this energy spread may also be investigated, however, this is less of a priority. Percentage energy spreads up to 80% were investigated without signs of alterations to the measured emittance of emittance measurement. It is expected that as the beam energy moves outside the  $0.28 \text{ GeV}$  to  $6 \text{ GeV}$  range, emittance measurements will become more erroneous since most of the beam will not hit the screen.

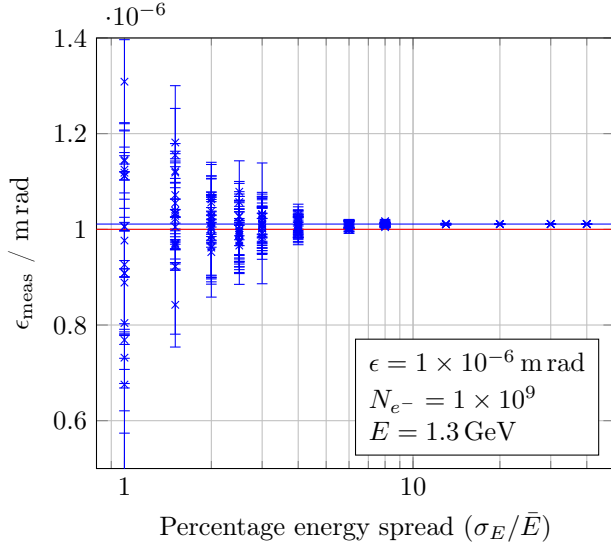


Figure 6: Plot of the simulated emittance measurement against the percentage spread of the beam energy, showing emittance measurements becoming unreliable at percentage energy spreads below 2%.

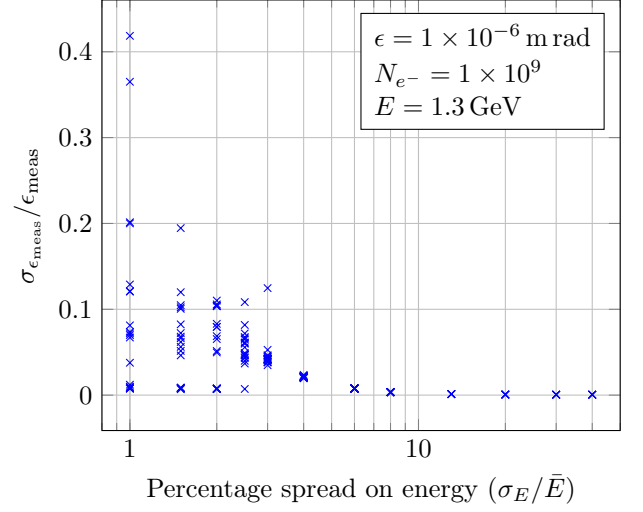


Figure 7: Plot of the simulated emittance measurement errors against the percentage spread of the beam energy, showing an exponential increase in the spread of the errors as the percentage error spread is narrowed.

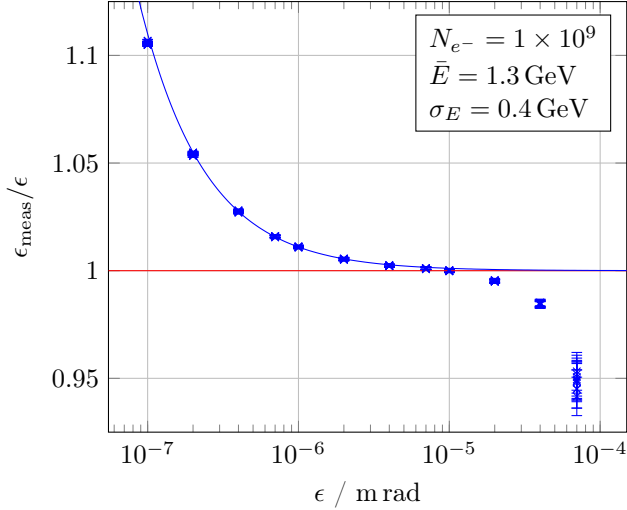


Figure 8: Plot of the ratio between the measured and true emittances of the beam against the true emittance of the beam. The blue line is the expected measurement value when taking into account the systematic overestimation due to discrete bins.

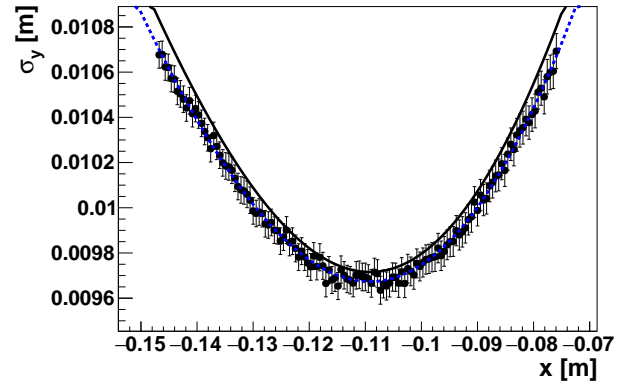


Figure 9: Beam reconstruction for a large beam emittance of  $7 \times 10^{-5} \text{ mrad}$  showing the underestimation of the measured vertical beam sizes.

### 7.3 Input Emittance

Since the emittance is the parameter required to be measured, a reasonably large region around the expected emittance should give precise emittance measurements. The input beam emittance range tested was from  $1 \times 10^{-7}$  mrad to  $1 \times 10^{-4}$  mrad as shown in Figure 8. Emittances below  $10^{-5}$  mrad showed accurate emittance measurements, with the  $\sim 10^{-8}$  mrad overestimation of the emittance measuring persisting over this range.

Increasing the emittance of the beam above  $10^{-5}$  mrad results in an underestimation in the measurement of the emittance as well as an increase in the measurement's error. This behaviour is expected. Increasing the emittance of the beam means the spread of the beam on the screen is larger. At emittances above  $10^{-5}$  mrad, a significant proportion of the beam's electrons no longer hit the 6.5 cm tall screen, so particles with the largest transverse momentum no longer contribute to the emittance measurement. Figure 9 displays this effect showing that the shape of the beam on the screen is a lot less focused in the vertical axis and each vertical beam size measurement is underestimated in comparison to the run of expected parameters in Figure 4.

### 7.4 Background Photons

This background noise is the most likely source of error to change during and between runs, as all other sources of error arise from intrinsic properties of the equipment, or from the setup of the experiment. The background photon noise is expected to be almost insignificant in comparison to the signal of the beam, where the ratio of signal to background photons is expected to be in the order of magnitude  $4 \times 10^4$ . The aim was to find the level of background photon radiation at which the measurement of the emittance would be strongly affected. The expected background density was multiplied by an arbitrary factor until the emittance value deviated from the true value. Figure 10 shows how this factor affects the measurement. Only after the expected background has been multiplied by a factor of  $\sim 100$  is any effect seen on the measured emittance. Between background factors  $10^2$  and  $10^3$  the measured emittance begins to be underestimated and above a background factor of  $10^3$  the emittance measurement becomes increasingly imprecise with a deviation a few

percent at a background factor of  $2 \times 10^3$ , increasing up to 10 % at a background factor of  $10^7$ .

The reasoning for a larger spread in the measured emittance values comes from the background drowning out the signal, that is, the fluctuations of the randomly generated background between the pixels become large enough to distort the shape of the image on the screen. The amount by which the image is distorted is not taken into account by the error bars suggesting that error in the background was not completely accounted for.

From both plots in Figure 10 and Figure 11 it is clear that the error bars do not take into account the fluctuations in the measured emittance between runs, or fluctuations in the measured vertical beam size. Error bars in Figure 10 can be inferred from the spread of the measurements since for lower backgrounds all ten runs are closely grouped and for higher backgrounds there is a clear spread of measurement values.

## 8 Conclusion

### 8.1 Errors

Despite accepting the error bars for many of the graphs, it is still likely that the calculation of the errors are wrong. Looking at the output files of simulations with very large backgrounds, it is clear that the error bars do not take into account the large statistical fluctuations about the expected beam size. The calculation of errors in the simulation is well understood apart from the calculation of the error of the  $\chi^2$  fitted parameters.

### 8.2 Parameters

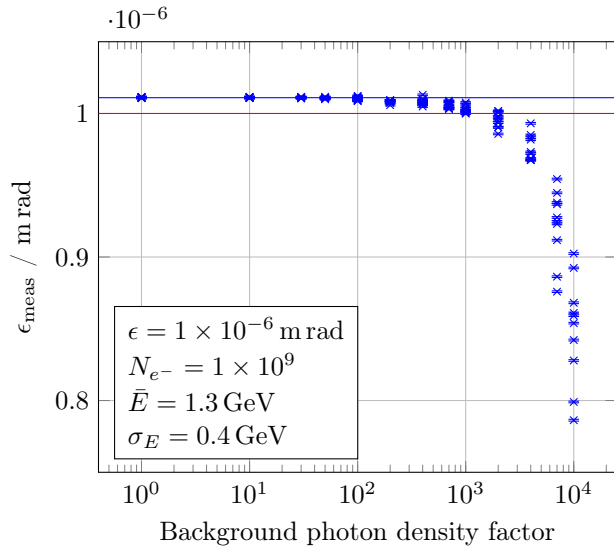


Figure 10: Plot of the measured beam emittance against a factor of the expected background density of  $3.415 \times 10^4 \text{ photons/m}^2$

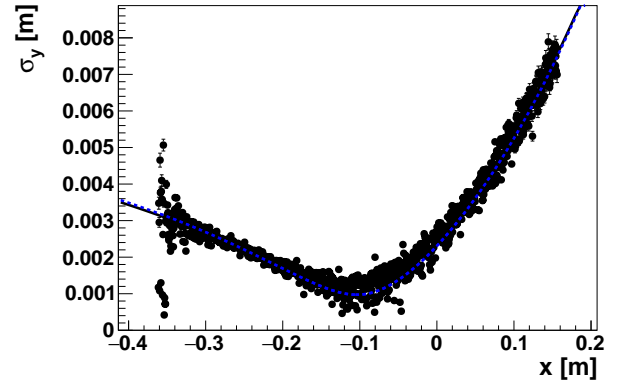


Figure 11: Beam reconstruction for a background  $1 \times 10^4$  times the expected background photon density.



## References

- [1] I Agapov et al. “BDSIM: A particle tracking code for accelerator beam-line simulations including particle-matter interactions”. In: *Nuclear Instruments and Methods in Physics Research Section A: Accelerators, Spectrometers, Detectors and Associated Equipment* 606.3 (2009), pp. 708–712.
- [2] Sea Agostinelli et al. “GEANT4 - A simulation toolkit”. In: *Nuclear instruments and methods in physics research section A: Accelerators, Spectrometers, Detectors and Associated Equipment* 506.3 (2003), pp. 250–303.
- [3] R. Barate et al. “Search for the standard model Higgs boson at LEP”. In: *Phys. Lett. B* 565 (2003), pp. 61–75. DOI: [10.1016/S0370-2693\(03\)00614-2](https://doi.org/10.1016/S0370-2693(03)00614-2). arXiv: [hep-ex/0306033](https://arxiv.org/abs/hep-ex/0306033) [hep-ex].
- [4] R. Brun and F. Rademakers. “ROOT: An object oriented data analysis framework”. In: *Nucl. Instrum. Meth.* A389 (1997), pp. 81–86. DOI: [10.1016/S0168-9002\(97\)00048-X](https://doi.org/10.1016/S0168-9002(97)00048-X).
- [5] Jean Buon. “Beam phase space and emittance”. In: *CERN European Organization for Nuclear Research-Reports-CERN* (1994), pp. 89–89.
- [6] CMS Collaboration. “First measurement of the differential cross section for  $t\bar{t}$  production in the dilepton final state at  $\sqrt{s} = 13$  TeV”. In: (2015).
- [7] E. Gschwendtner et al. “AWAKE, The Advanced Proton Driven Plasma Wakefield Acceleration Experiment at CERN”. In: *Nucl. Instrum. Meth.* A829 (2016), pp. 76–82. DOI: [10.1016/j.nima.2016.02.026](https://doi.org/10.1016/j.nima.2016.02.026). arXiv: [1512.05498](https://arxiv.org/abs/1512.05498) [physics.acc-ph].
- [8] *Hardware Guide for the iStar Intensified sCMOS camera*. Version 1 rev 19. ANDOR an Oxford Instruments company. Andor Technology Ltd., 7 Millennium Way, Springvale Business Park, Belfast, BT12 7AL, Northern Ireland, Sept. 2016.
- [9] Naveen Kumar, Alexander Pukhov, and Konstantin Lotov. “Self-modulation instability of a long proton bunch in plasmas”. In: *Physical review letters* 104.25 (2010), p. 255003.
- [10] Wim P. Leemans et al. “GeV electron beams from a cm-scale accelerator”. In: *Nature Phys.* 2 (2006), pp. 696–699. DOI: [10.1038/nphys418](https://doi.org/10.1038/nphys418).
- [11] KV Lotov et al. “Natural noise and external wakefield seeding in a proton-driven plasma accelerator”. In: *Physical Review Special Topics-Accelerators and Beams* 16.4 (2013), p. 041301.
- [12] W. Lu et al. “Generating multi-GeV electron bunches using single stage laser wakefield acceleration in a 3D nonlinear regime”. In: *Phys. Rev. ST Accel. Beams* 10 (2007), p. 061301. DOI: [10.1103/PhysRevSTAB.10.061301](https://doi.org/10.1103/PhysRevSTAB.10.061301). arXiv: [physics/0612227](https://arxiv.org/abs/physics/0612227) [physics].
- [13] E Oz and P Muggli. “A novel Rb vapor plasma source for plasma wakefield accelerators”. In: *Nuclear Instruments and Methods in Physics Research Section A: Accelerators, Spectrometers, Detectors and Associated Equipment* 740 (2014), pp. 197–202.
- [14] Erdem Oz, Fabian Batsch, and Patric Muggli. “A Novel Laser Ionized Rb Plasma Source for Plasma Wakefield Accelerators”. In: *Proceedings, 5th International Particle Accelerator Conference (IPAC 2014): Dresden, Germany, June 15-20, 2014*. 2014, TUPME073. URL: <http://jacow.org/IPAC2014/papers/tupme073.pdf>.
- [15] Carl Siemon et al. “Laser-seeded modulation instability in a proton driver plasma wakefield accelerator”. In: *Physics of Plasmas (1994-present)* 20.10 (2013), p. 103111.
- [16] A. A. Sokolov and I. M. Ternov. “Synchrotron radiation”. In: *Akademia Nauk SSSR, Moskovskoie Obshchestvo Ispytatelei*

*prirody. Sektsia Fiziki. Sinkhrotron Radiation, Nauka Eds., Moscow, 1966 (Russian title: Sinkhrotronnoie izluchenie), 228 pp. (1966).*

- [17] T. Tajima and J. M. Dawson. “Laser electron accelerator”. In: *Phys. Rev. Lett.* 43 (1979), pp. 267–270. DOI: [10.1103/PhysRevLett.43.267](https://doi.org/10.1103/PhysRevLett.43.267).
- [18] J Vieira, WB Mori, and P Muggli. “Hosing instability suppression in self-modulated plasma wakefields”. In: *Physical Review Letters* 112.20 (2014), p. 205001.
- [19] J. Vieira et al. “Ion motion in the wake driven by long particle bunches in plasmas”. In: *Phys. Plasmas* 21 (2014), p. 056705. DOI: [10.1063/1.4876620](https://doi.org/10.1063/1.4876620). arXiv: [1409.4328 \[physics.plasm-ph\]](https://arxiv.org/abs/1409.4328).
- [20] J. Vieira et al. “The ion motion in self-modulated plasma wakefield accelerators”. In: *Phys. Rev. Lett.* 109 (2012), p. 145005. DOI: [10.1103/PhysRevLett.109.145005](https://doi.org/10.1103/PhysRevLett.109.145005). arXiv: [1208.3242 \[physics.plasm-ph\]](https://arxiv.org/abs/1208.3242).
- [21] Helmut Wiedemann. *Particle accelerator physics I*. Berlin, Germany: Springer, 1999. ISBN: 9783540490432, 9783662038277. DOI: [10.1007/978-3-662-03827-7](https://doi.org/10.1007/978-3-662-03827-7). URL: <http://www.springer.com/us/book/9783662038277>.